Article

RADAR-Vegetation Structural Perpendicular Index (R-VSPI) for the Quantification of Wildfire Impact and Post-Fire Vegetation Recovery

Aakash Chhabra [1], Christoph Rüdiger [1,2,*], Marta Yebra [3,4], Thomas Jagdhuber [5,6] and James Hilton [7]

1　Department of Civil Engineering, Monash University, Clayton, VIC 3800, Australia;
　　aakash.chhabra@monash.edu
2　Bureau of Meteorology, Docklands, VIC 3008, Australia
3　Fenner School of Environment & Society, College of Science, The Australian National University,
　　Canberra, ACT 2600, Australia; marta.yebra@anu.edu.au
4　School of Engineering, College of Engineering and Computer Science, The Australian National University,
　　Canberra, ACT 2600, Australia
5　Microwaves and Radar Institute, German Aerospace Center (DLR), 82234 Wessling, Germany;
　　thomas.jagdhuber@dlr.de
6　Institute of Geography, Faculty of Applied Informatics, Augsburg University, 86159 Augsburg, Germany
7　Data-61, Commonwealth Scientific and Industrial Research Organisation, Clayton, VIC 3168, Australia;
　　james.hilton@data61.csiro.au
*　Correspondence: christoph.rudiger@bom.gov.au

Abstract: The precise information on fuel characteristics is essential for wildfire modelling and management. Satellite remote sensing can provide accurate and timely measurements of fuel characteristics. However, current estimates of fuel load changes from optical remote sensing are obstructed by seasonal cloud cover that limits their continuous assessments. This study utilises remotely sensed Synthetic-Aperture Radar (SAR) (Sentinel-1 backscatter) data as an alternative to optical-based imaging (Sentinel-2 scaled surface reflectance). SAR can penetrate clouds and offers high-spatial and medium-temporal resolution datasets and can hence complement the optical dataset. Inspired by the optical-based Vegetation Structural Perpendicular Index (VSPI), an SAR-based index termed RADAR-VSPI (R-VSPI) is introduced in this study. R-VSPI characterises the spatio-temporal changes in fuel load due to wildfire and the subsequent vegetation recovery thereof. The R-VSPI utilises SAR backscatter ($\sigma°$) from the co-polarized (VV) and cross-polarized (VH) channels at a centre frequency of 5.4 GHz. The newly developed index is applied over major wildfire events that occurred during the "Black Summer" wildfire season (2019–2020) in southern Australia. The condition of the fuel load was mapped every 5 (any orbit) to 12 (same orbit) days at an aggregated spatial resolution of 110 m. The results show that R-VSPI was able to quantify fuel depletion by wildfire (relative to healthy vegetation) and monitor its subsequent post-fire recovery. The information on fuel condition and heterogeneity improved at high-resolution by adapting the VSPI on a dual-polarization SAR dataset (R-VSPI) compared to the historic forest fuel characterisation methods (that used visible and infrared bands only for fuel estimations). The R-VSPI thus provides a complementary source of information on fuel load changes in a forest landscape compared to the optical-based VSPI, in particular when optical observations are not available due to cloud cover.

Keywords: microwave remote sensing; synthetic aperture radar; Sentinel-1; Sentinel-2; wildfire; fuel mapping; vegetation recovery

1. Introduction

Wildfires are a global phenomenon that causes disturbances across terrestrial ecosystems and plays a critical role in altering Earth's carbon and water cycle [1]. Recent studies indicate that around the globe wildfires burn nearly 423 Mha yr^{-1} [2] of vegetated land

with the majority in open landscapes, such as grasslands and savannahs [3]. However, most ecological biomes are affected by wildfire at some point in time. In a global context, Australia has one of the highest wildfire incident rates [4]. Given the ascendency of wildfire-prone and -reliant vegetation across the Australian landscape ranging from closed-canopy forests, savannas, and grasslands to sparsely vegetated deserts, Australia is the ideal location to investigate the wildfire regimes at a continental scale. Over the past millennia, wildfires have played a significant role in shaping the distribution and arrangement of Australian vegetation, in particular in south-eastern Australia. Wildfire regimes in these regions have the potential to occur at higher intensities and more frequently than in other parts of Australia [5] and possibly even the world [6].

Due to the extreme consequences of wildfires, estimating and forecasting wildfire risk [7,8] is critical. Wildfire risk depends mainly on three measures—the availability of ignition sources, fuel conditions (fuel load and structural distribution and connectivity, and moisture content), which determine the availability and tendency of the vegetation fuel to burn, and the ease of wildfire spread once the wildfire has ignited [9,10]. This is further influenced by the local topography, as well as preceding and current weather conditions. In southern Australia, eucalypt forests are the most dominant woody vegetation. The fuel load in these fire-prone forests is largely characterised by overstory trees, intermediate trees, elevated fuel layer, near-surface fuels, and surface fuels [11]. The fuel load characteristics in eucalypt forests affect fire spread, flame height, and fire duration and intensity [11]. Even though fuel load strongly enhances the wildfire risk, its spatio-temporal variability remains poorly understood. Thus, long-term time-series maps of fuel load and conditions are an important factor in advancing the knowledge in spatio-temporal characteristics and improving the wildfire risk predictions. Many operational wildfire models principally rely on meteorological datasets (wind, temperature, humidity, precipitation), as well as topography and modelled fuel characteristics, which are often only coarsely mapped in their spatial and temporal resolutions [12–16]. Consequently, predictions of wildfire spread from these models are less accurate than the predictions from wildfire models that use fuel datasets of high quality [17–19].

In the past, there has been a reliance on visual, field-based methods to assess the fuel load condition, composition, structure, and re-accumulation following a wildfire [20]. These methods were often subjective and could only be implemented across small areas, given their stochastic spatio-temporal nature that would require substantial areas to be monitored [21]. Therefore, a dataset that considers the spatio-temporal variability of the re-accumulated fuel load (post-fire), over a large geographic extent is unfeasible to obtain using conventional field survey methods [22].

In contrast to these traditional methods, space-borne remote sensing can provide continuous datasets for analysing and monitoring the changing fuel conditions for any location from regional to continental scales [23]. Broadband optical sensors, such as those onboard the National Aeronautics Space Administration (NASA)'s Landsat missions and the European Space Agency (ESA)'s Sentinel-2 mission, provide observations useful to resolve part of this complexity because of acquisitions at sufficient spatial and temporal resolutions. Numerous studies have investigated vegetation characteristics in different forest biomes, such as temperate [24,25], boreal [26], Mediterranean [27,28], and eucalypt [29] forests. Spectral indices, such as the Normalized Difference Vegetation Index (NDVI) [30], Normalized Burn Ratio (NBR) [31], and differenced NBR (dNBR) [32], have been extensively used for assessing the vegetation condition related to the quantification of the current state of the fuel or the wildfire severity itself.

In NBR, near-infrared (NIR) is mostly sensitive to the lignin and the shortwave-infrared (SWIR) wavelength is sensitive to water absorption [32]. Since NBR is based on those wavelengths, it is only sensitive to the changes in the leaf structure and density and overlooks the changes in fuel structure and recovery [33]. NBR's modified version, dNBR, provides a relative metric of change compared to pre-fire conditions. Since the dNBR index provides a measure of change in vegetation due to wildfire, it fails to consider the

heterogeneous description of the vegetation. That is, for the same intensity of burn, a pixel with sparse pre-fire vegetation will measure lower dNBR (small change). However, a pixel with dense pre-fire vegetation will display a higher dNBR (higher change) [34]. Thus, for the areas with diverse vegetation strata and densities, mapping vegetation characteristics is challenging [35]. On the other hand, Massetti et al. [29] introduced a multi-spectral index called Vegetation Structure Perpendicular Index (VSPI) that incorporates the SWIR-1 (1.6 μm) and SWIR-2 (2.2 μm) bands of the Landsat 8 satellite. The results showed that VSPI was able to observe the spatio-temporal disturbance in fuel loads over a longer period when compared to NDVI and NBR. The main shortcomings of the methods discussed above stems from optical remote sensing being affected by the presence of cloud cover, which means that continuous monitoring of vegetation characteristics is adversely impacted, leading to temporal gaps in the time series. Moreover, the dense canopy of the forests along with its shadows obstructs the reflectance signal from optical sensors to accurately map vegetation characteristics [36], especially from the understorey.

Radar sensors have the potential to overcome some of the drawbacks of optical remote sensing and offers a complementary approach to continuously monitoring the biomass, state of disturbed vegetation, and post-fire recovery due to its all-weather, and day–night imaging capability [37–39]. A radar sensor is an active sensor that uses a system mode called Synthetic Aperture Radar (SAR). SAR works on microwave signals that are at least four orders of magnitude longer than the optical [40]. Consequently, these recorded signals saturate less at higher biomass levels [41] and can penetrate through clouds [42] and dense canopies [43], unlike optical remote sensing. However, SAR generates high-resolution imagery that is highly influenced by speckle noise and soil moisture content (depending on canopy penetration), and, therefore, requires separate methods to account for the variations of soil moisture content [44]. The application of SAR to burnt area studies is defined by changes in backscatter due to loss in vegetation structure by wildfire. These variations in backscatter are directly proportional to the degree of burn, and thus enable SAR to detect wildfire scars and monitor post-fire regrowth [45,46]. Determining the impact of the fire and monitoring the post-fire regrowth of the forest fuel load using SAR is not a novel approach, however; it is a new application area with a limited number of studies [37,38,43,45,47].

To date, very few studies have continually updated large scale maps on the structure of the forest vegetation in an Australian context by using optical remote sensing [29] and microwave remote sensing [48]. Given that the channels with longer wavelengths can better capture the standing woody material [49], this study aims to expand the use of the VSPI [29] and apply it to the time-series of independent sensors—Sentinel-1 (10 m; before speckle reduction) and Sentinel-2 (20 m)—to produce high-resolution forest vegetation condition maps that provide a better measure of depletion in fuel structure relative to healthy vegetation and its subsequent recovery to the original state, with a temporal resolution between 5 (Sentinel-2) and 12 (Sentinel-1) days. With this background in mind, the robustness of the new index, i.e., RADAR-VSPI (R-VSPI), is tested and compared with VSPI across various wildfires in different parts of southern Australia.

2. Materials and Methods

2.1. Optical- and SAR-Based VSPI

A major application of remote sensing in wildfire ecology studies includes burn severity mapping, i.e., the provision of fuel depletion measures due to a wildfire. Kollenkark et al. [50] have shown that the spectral data collected from optical remote sensing often represent a convoluted mixture of vegetation properties, soil background, shadow etc. As a consequence, NIR-SWIR reflectance-based indices that have been developed to quantify the impact of wildfire on fuel load are limited in their capacity. Massetti et al. [29] estimated changes in fuel structure in a forest due to wildfire using orthogonal transformations to estimate the perpendicular deviation of the signal from a standard reference, based on a two-dimensional perpendicular vegetation index (PVI) [51]. The authors computed a vegetation line formed by an assumed linear relationship between the scaled surface reflectance values acquired

from two SWIR channels (1.6 μm and 2.2 μm) over healthy vegetation (Figure 1a). The vegetation line is assembled using a linear function, where m and c are the slope and intercept, respectively. The line characterises the spatio-temporal conditions of the forest vegetation not affected by external disturbances, such as wildfires or clearing. The disturbances caused by wildfires come with a change in water content and structure, which shifts the scaled surface reflectance values of the paired dataset to another line (Figure 1a). With time, the scaled surface reflectance values from the disturbed vegetation return progressively to the pre-disturbance state due to the recovery in vegetation (Figure 1c). The VSPI for disturbance A is then computed as the orthogonal distance in between the vegetation line and the point A (x_A, y_A) in the 2-D space [52]:

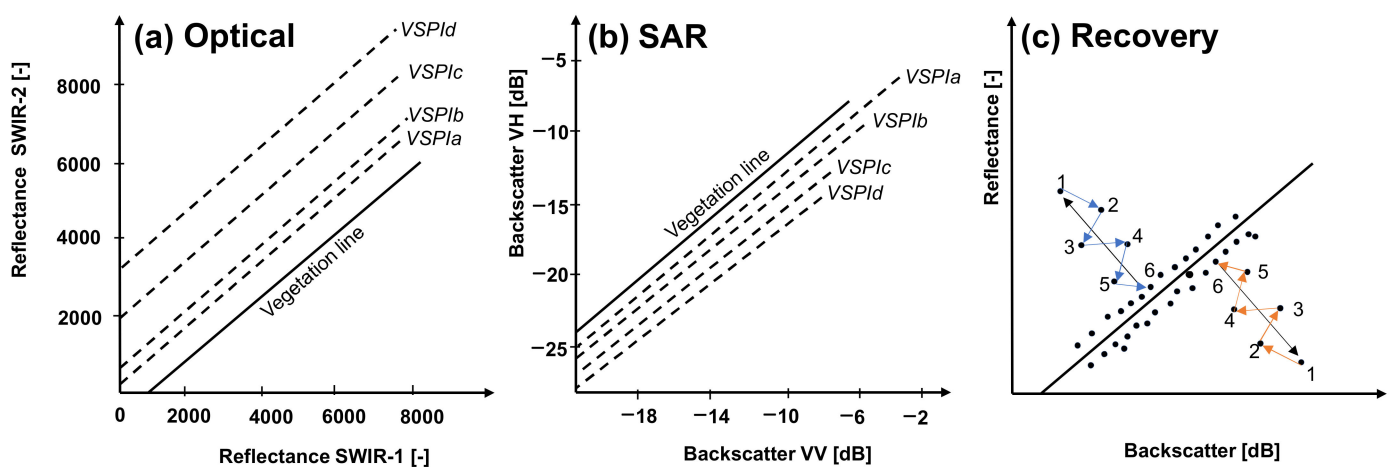$$\text{VSPI}_A = \frac{1}{\sqrt{m^2 + 1}} \times (y_A - mx_A - c) \tag{1}$$

Figure 1. Illustration of VSPI on optical (**a**), SAR (**b**). The solid line represents the healthy vegetation, whereas the dashed isolines (VSPIa, VSPIb, VSPIc, VSPId) represents the orthogonally displaced vegetation point due to external disturbances, such as wildfires. The optical values of SWIR-1 and SWIR-2 bands are expressed as scaled surface reflectance in linear units, whereas the SAR values of VH and VV polarization channels are expressed in dB scale. (**c**) Schematic illustration of undisturbed vegetation (dots along the vegetation line) and the recovery of the disturbed vegetation to the pre-fire state; from point 1 to 6 for Optical (blue) and SAR (Orange) data. Illustrations in Figure 1a,c are adapted from [29].

As an analogue to the vegetation line computed using optical signals, a linear relationship between the backscatter from co-polarized (VV) and cross-polarized (VH) channels is hypothesised (Figure 1b). While SAR signals observed over forests are inherently complex observations that are affected by the various physical properties of the target, the simplifying assumption here is that the backscatter from VV is predominantly sensitive towards surface scattering components (such as the landscape moisture), whereas the energy measured from the VH (i.e., measuring energy returning at a 90° offset to the transmitting wave) is largely a function of the volume scattering [53], i.e., the structure of the vegetation. Thus, in this hypothesis for tracking forest degradation, cross-polarized observations from SAR are termed on the y-axis. The method for the calculus of the vegetation line and the computation of the orthogonal distance remains the same as discussed above. It is expected and will in fact be shown that these assumptions hold reasonably well for forests but may require further investigation for different vegetation types, such as shrublands [54].

2.2. Study Area and Wildfires

Five wildfires were selected in four different states and territories (denoted as 'study areas') to assess the performance of R-VSPI and VSPI from Sentinel-1 and Sentinel-2 datasets, respectively (Table 1, Figure 2). The wildfires occurred during the 2019–2020 "Black Sum-

mer" wildfire season (between September 2019 and March 2020) in south-eastern and south-western Australia, including the Australian Capital Territory (ACT), New South Wales (NSW), Victoria (VIC), and Western Australia (WA). The study areas are characterised by temperate climate zone and native vegetation, such as forest and woodlands of eucalyptus types combined with grasslands and heathlands [55], qualifying it as an excellent location for the study.
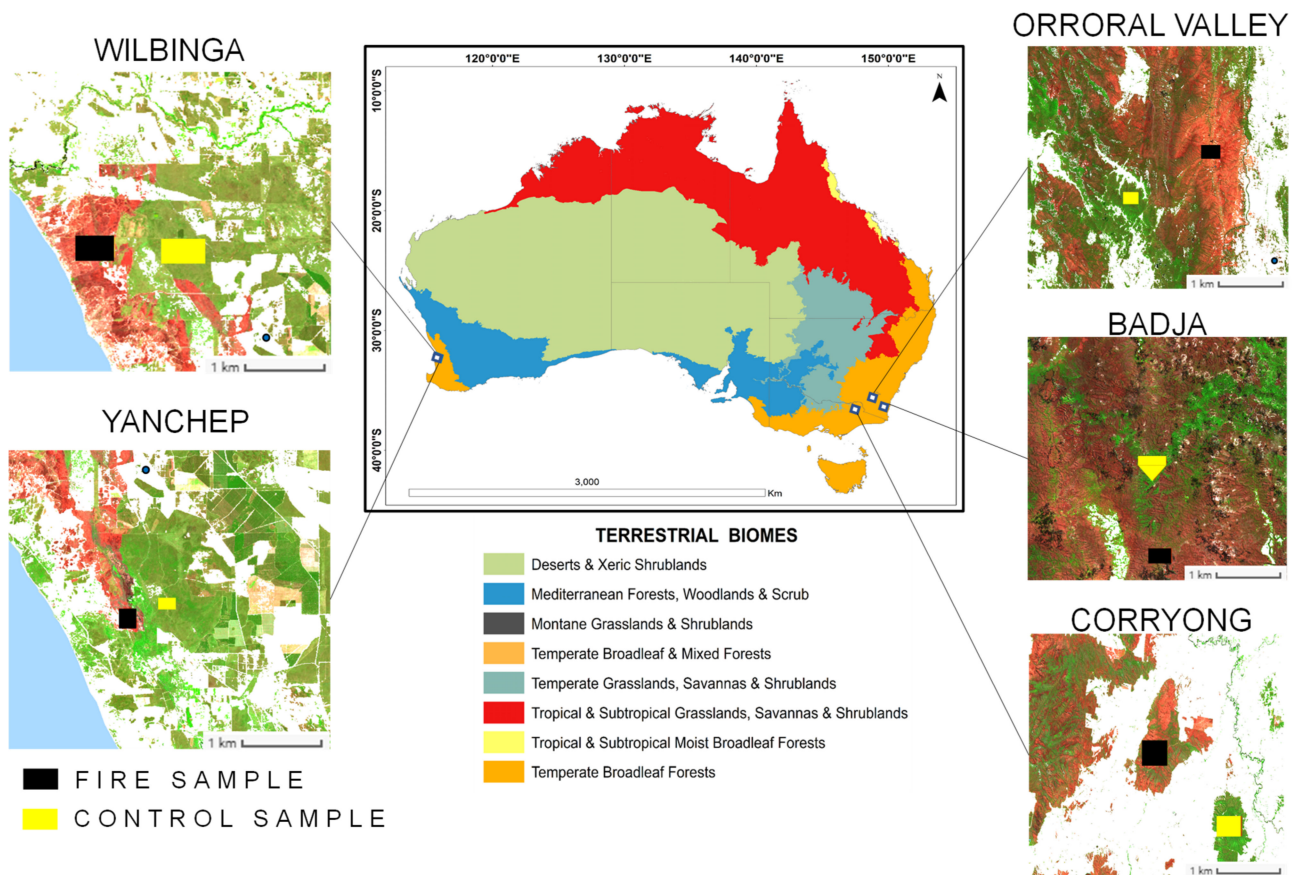

Figure 2. Overview of different terrestrial biomes [56] and five wildfires. The illustrations represent the fire sample (black) and control sample (yellow) masks for wildfires in VIC (Victoria), NSW (New South Wales), ACT (Australian Capital Territory), and WA (Western Australia). The base maps are Band12/Band 8/Band 4 infrared colour composites of the Sentinel-2 acquisition of the nearest date (post-fire) to the wildfire event (Table 1).

Table 1. Characteristics of the five wildfires that were analyzed across four different study areas in Australia [57]. The total number of available Sentinel-1 (S1) and Sentinel-2 (S2) satellite scenes, date and location of the wildfires, and closest scene to the wildfire are also shown, as well as the size of the wildfire and control samples. Terrestrial biomes are a representation from [56].

Date	Location	Closest Satellite Acquisition (Post-Fire)		Extent (Ha)	Sampling Area		Number of Scenes		Terrestrial Biomes
		S1	S2		Wildfire Sample (Ha)	Control Sample (Ha)	S1	S2	
29 December 2019–late January 2020	Corryong (VIC)	10 January 2020	8 January 2020	110,000	480	373	117	94	Temperate broadleaf forests (wet sclerophyll)

Table 1. *Cont.*

Date	Location	Closest Satellite Acquisition (Post-Fire)		Extent (Ha)	Sampling Area		Number of Scenes		Terrestrial Biomes
		S1	S2		Wildfire Sample (Ha)	Control Sample (Ha)	S1	S2	
27 December 2019–30 December 2019	Badja Forest (NSW)	5 January 2020	10 January 2020	315,000	457	620	115	71	Temperate broadleaf forests (wet sclerophyll)
27 January 2020–17 February 2020	Orroral Valley (ACT)	8 February 2020	4 February 2020	87,000	316	226	232	56	Temperate broadleaf forests (wet sclerophyll)
11 December 2019	Yanchep (WA)	19 December 2019	18 December 2019	11,500	280	362	125	87	Temperate broadleaf forests (dry sclerophyll)
15 December 2019	Wilbinga (WA)	18 December 2019	18 December 2019	6500	404	481	125	87	

The "Black Summer" wildfire season was exceptional in terms of area burnt and wildfire severity [58–61]. These mega wildfires had a devastating and direct impact on the ecosystems, humans, and economy. The Black Summer wildfires eventually resulted in the burning of 24 million hectares of mainly native forests, i.e., 50 times larger than California's most extensive wildfire ever recorded [62] and five times more extensive than the size of the 2019 wildfires in the Amazon [63], and led to extremely poor air quality in major cities [64,65].

2.3. Sentinel Constellation Time-Series Dataset

This study utilises the Copernicus Sentinel-1 C-band (5.4 GHz) dual-polarization data, i.e., vertical–vertical (VV) and vertical–horizontal (VH), in Interferometric Wide swath (IW) mode [66]. The native spatial resolution in IW-mode is 5 m × 20 m. A continuous-time series was obtained from Google Earth Engine for the period 1 January 2017 to 31 January 2021 (Table 1) with repeat overpasses every 5 days (any orbit) and 12 days (same orbit) over Australia. This imagery collection includes the SAR-Ground Range Detected (GRD) scenes that have been pre-processed (steps: application of orbit file, thermal noise removal, radiometric calibration, and terrain correction) using ESA's Sentinel-1 toolbox to produce a calibrated and ortho-rectified product with normalized backscattering coefficients (σ°) in dB scale [67]. The Sentinel-1 images have a data-inherent granular appearance, which is due to speckle noise. To reduce this, a bilinear interpolation algorithm [68] was applied, before resampling (by ways of averaging) the data from its native resolution to 110 m × 110 m pixels.

The Copernicus Sentinel-2 (S2) mission provides a high-resolution dataset with a global 5-day temporal resolution. The multispectral imager (MSI) on-board S2 acquires measurements in 13 spectral bands, including visible and NIR at 10 m, and SWIR at 20 m [69]. These are commonly used bands of the electromagnetic spectrum for studying the characteristics of vegetation-, soil-, and wildfire-related parameters in the optical domain. This study uses the Level-2A (L2A) orthorectified, atmospherically corrected scaled surface reflectance time series available from 1 December 2018 to 31 January 2021 (Table 1) [70]. The scaled surface reflectance values were taken from the SWIR-1 and SWIR-2 channels from every Sentinel-2 image acquisition that fitted the cloud percentage (<20%) criteria. The scaled surface reflectance values were filtered for snow, water, cirrus, and cloud shadow using a quality assessment band.

2.4. Computation of Indices

The reference lines of the VSPI were computed using all available pre-fire data. The VSPI was subsequently determined for all dates and scenes as the orthogonal distance from the reference line (Equation (1)) with m and c as the slope and the intercept parameters

of the reference line, and x and y as the scaled surface reflectance values of SWIR-1 and SWIR-2 bands of Sentinel-2. Similar to the VSPI calculated with the Sentinel-2 data, the R-VSPI was estimated for all dates and scenes as the orthogonal distance from the reference line (Equation (1)) where the x- and y-values were set to be the backscatter values of VV and VH polarization channels of Sentinel-1, respectively.

The Sentinel-2 -based NBR and dNBR were calculated as follows,

$$NBR = (NIR - SWIR2)/(NIR + SWIR2) \tag{2}$$

$$dNBR = NBR_{PRE} - NBR_{POST} \tag{3}$$

while the NDVI is the normalized difference vegetation index measured between the pixel values of NIR and Red-edge bands:

$$NDVI = (NIR - Red)/(NIR + Red) \tag{4}$$

The Radar Forest Degradation Index (RFDI) [53,71] as well as the co-polarized to the cross-polarized (VV/VH) ratio [72], were computed with Sentinel-1 data. Since the Sentinel-1 data does not offer HH and HV polarization channels, the RFDI was modified to use VV for HH and VH for HV (Equation (5)). This modified RFDI (mRFDI) is generally computed using intensity values [73]. mRFDI is designed to detect structural changes and recovery in a forest. The values of mRFDI range from 0 to 1, where values nearing 0 indicate undisturbed forest structure and values nearing 1 indicate highly disturbed forest structure.

$$mRFDI = (\sigma^{\circ}_{VV} - \sigma^{\circ}_{VH})/(\sigma^{\circ}_{VV} + \sigma^{\circ}_{VH}) \tag{5}$$

The mean of all pixels within the wildfire boundary was computed for every available acquisition date. A vegetation mask was used at 25-m resolution across the Australian continent [48]. For the identification of pixels from burnt areas, the extent of all the wildfires was manually delineated by photointerpretation of Sentinel-2 colour composites (Red: B2.2, Green: B0.84, Blue: B0.67). The control samples were undisturbed forests areas that offered reference forest conditions as a benchmark during the recovery of burnt areas. The control samples were selected from the unburnt forest (geographically near to the burnt area; Figure 2) and were monitored throughout the time series to be consistently unburnt and undisturbed.

3. Results and Discussion

3.1. Sentinel-1 Analysis

3.1.1. Vegetation Lines from Sentinel-1

Figure 3 shows the multi-temporal correlation plots and subsequent vegetation lines for the five wildfires derived from the backscatter values of the Sentinel-1 datasets. The regression slopes obtained for the Sentinel-1 data ranged from 0.82 to 1.1 for the different fires (Figure 3). The slopes of the vegetation line derived from Sentinel-1 data showed variation in the different study areas as the density and structure in the broader expanse of eucalypt forests vary significantly [74]. In that sense, the slope for Wilbinga was the lowest compared to all wildfires (Figure 3).
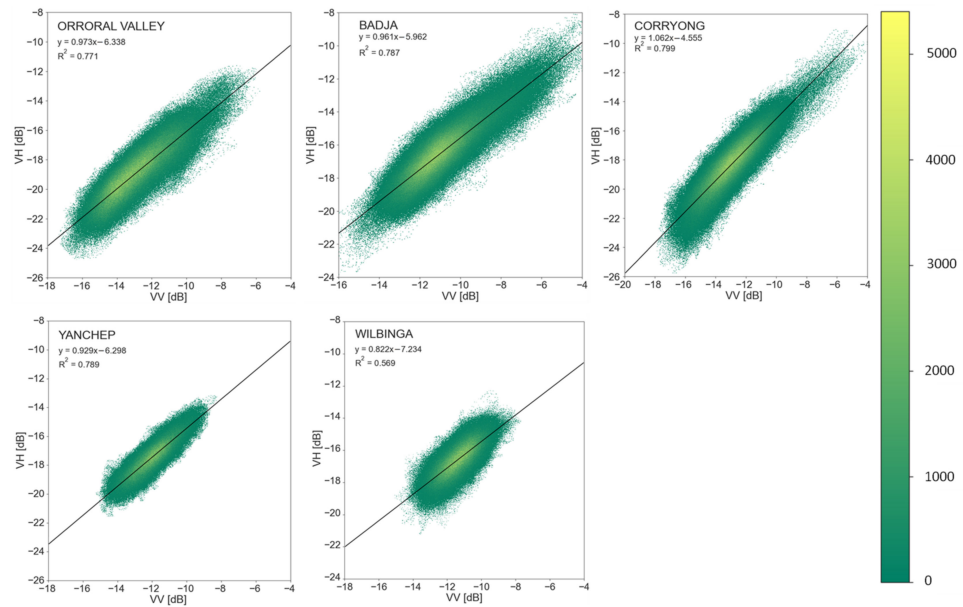
Figure 3. Density plots and vegetation lines from the backscatter values in the VV and VH bands from Sentinel-1 for the study areas Orroral Valley (Australian Capital Territory), Badja (New South Wales), Corryong (Victoria), Yanchep (Western Australia), and Wilbinga (Western Australia).

Figure 4a illustrates an example of the (non-burnt) vegetation line (black) and the displaced burnt-area lines (colored) for the Orroral Valley wildfire (ACT) using backscatter values from Sentinel-1. The vegetation line (black) obtained from the paired backscatter values over the forest areas from the pre-fire period represents undisturbed healthy vegetation (Figure 4a). The disturbance caused by wildfires, shifted the post-fire backscatter values away from the reference (vegetation) line, indicating the depletion of the forest fuel or change in the vegetation structure due to wildfire impact (Figure 4a). For the immediate post-fire period, the displaced isolines formed from the post-fire backscatter values of Sentinel-1 showed a clear, negative displacement from the vegetation line (Figure 4a). This is in accordance with the hypothesis (Figure 1B,C).
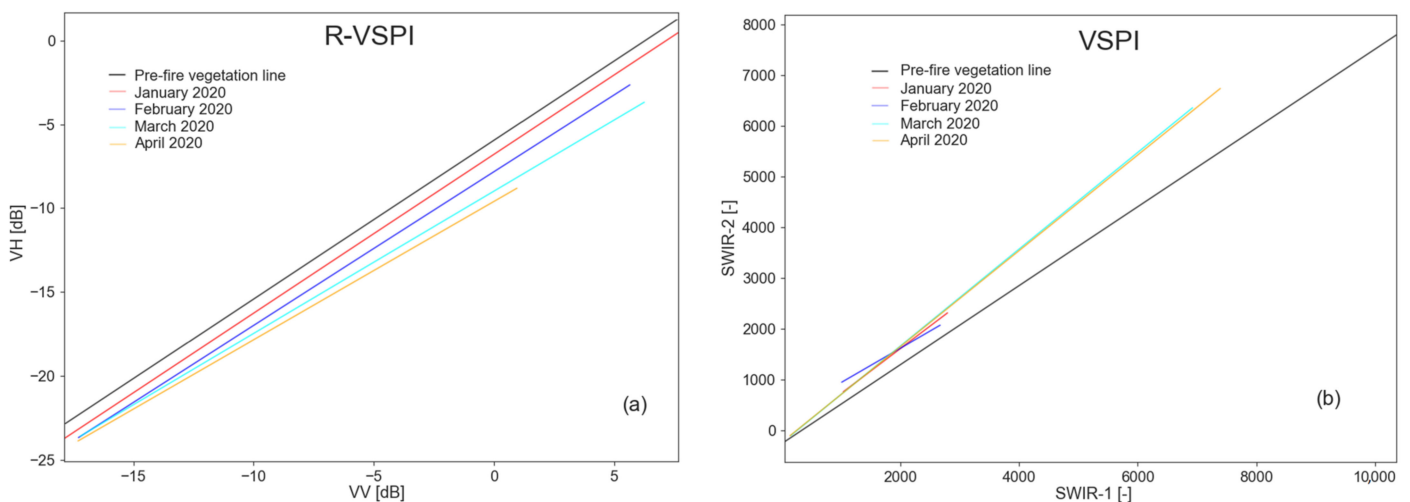

Figure 4. Illustration of vegetation and burnt area lines from (**a**) Sentinel-1 and (**b**) Sentinel-2 scaled surface reflectance data for the Orroral Valley wildfire. The solid line (black) represents the healthy vegetation, whereas the coloured solid isolines represents the displaced vegetation line during the post-fire months. The optical values of SWIR-1 and SWIR-2 bands are expressed in scaled surface reflectance values (unitless), whereas the backscatter values of VH and VV polarization channels are expressed in dB scale.

3.1.2. Analysis of Temporal Patterns from Sentinel-1

All indices computed from Sentinel-1 (R-VSPI, mRFDI, and VV/VH ratio) can distinguish disturbances caused by wildfire events from the undisturbed vegetation through a clear deviation in the spectral indices from their original reference (Figures 5a and 6). In addition, they also allow for the assessment and monitoring of the post-fire recovery of the burnt vegetation (Figures 5a and 6). The R-VSPI and mRFDI values for the Orroral Valley wildfire report that the disturbed vegetation still has not fully recovered to the level of the pre-fire period after 11 months (Figure 5a). For the same wildfire event and within the same time period the VV/VH ratio showed recovery of the vegetation by approaching the control sample and the pre-fire conditions (Figure 5a). A similar trend was also observed for the Corryong wildfire (Figure 6). The faster recovery using the ratio may have resulted due to the fact that the R-VSPI and mRFDI are more complex mathematical descriptors than a simple linear ratio. However, for the Yanchep wildfire in WA, all three indices, i.e., R-VSPI, mRFDI, and VV/VH ratio, showed post-fire vegetation recovery as the signals approached the control after 11 months (Figure 6).
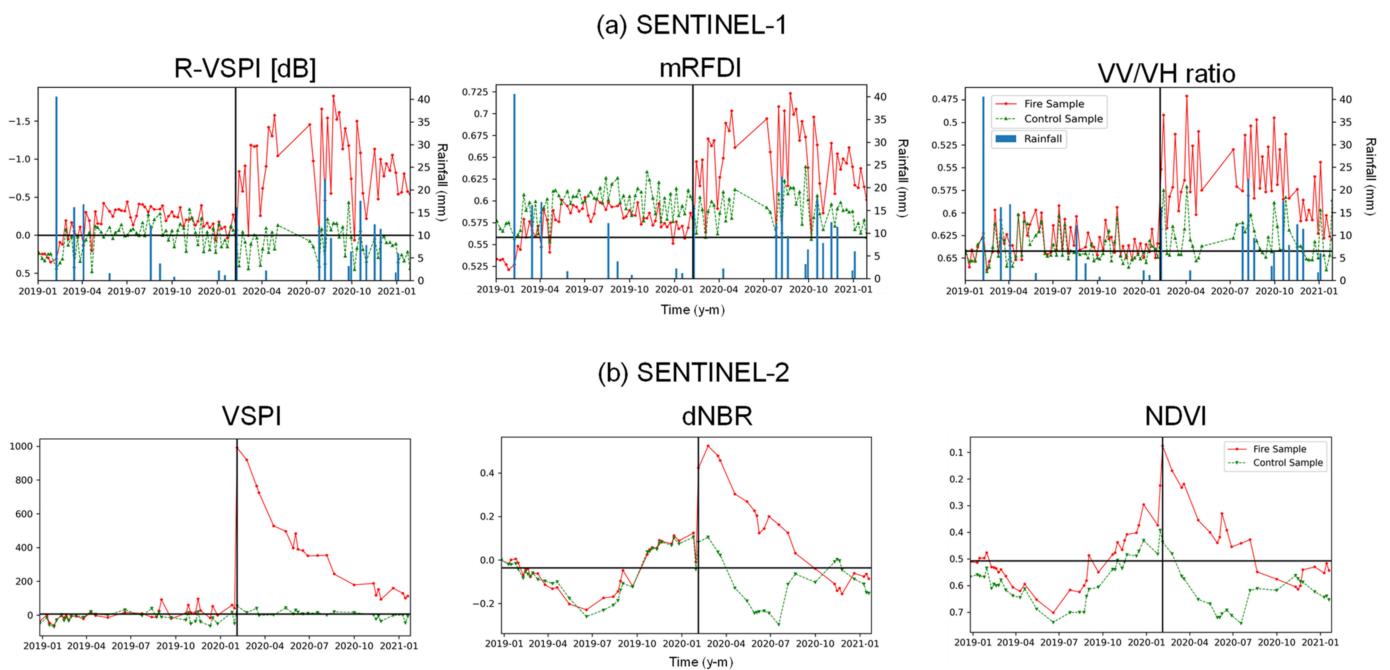

Figure 5. (**a**) Two-year time series of R-VSPI, mRFDI, and VV/VH ratio using Sentinel-1 backscatter dataset for Orroral Valley wildfire (ACT); (**b**) two-year time series of VSPI, dNBR, and NDVI using Sentinel-2 scaled surface reflectance dataset for Orroral Valley wildfire (ACT). Data are shown for burnt/wildfire samples (red) and control samples (green). The black lines indicate the latest imagery post the wildfire event (vertical) and pre-fire conditions (horizontal, mean of the wildfire sample taken pre-fire). The rainfall data is shown in column bars (blue).

Generally, the R-VSPI control samples marginally fluctuated around a steady-state value of zero, whereas the control sample values of mRFDI and VV/VH ratio showed a much higher relative variability within ranges of 0.5–0.8 and 0.5–0.7, respectively (Figures 5a and 6). It was also noticed that the post-fire signal from R-VSPI, mRFDI, and VV/VH ratio for all five wildfires showed significant noise (Figures 5a and 6), which was likely due to the effect of moisture from rainfall in and around the period of the satellite pass (Bragg scattering is the main physical mechanism generated by the raindrops impacting the surface, increasing the C-band SAR backscatter; [75]) and, subsequently, high levels of soil surface wetness [43,76].

Seasonal patterns in the control sample plots of R-VSPI and mRFDI are visible in the time series of the Orroral Valley, Corryong, Badja, and Yanchep burnt areas, except for the Wilbinga area.
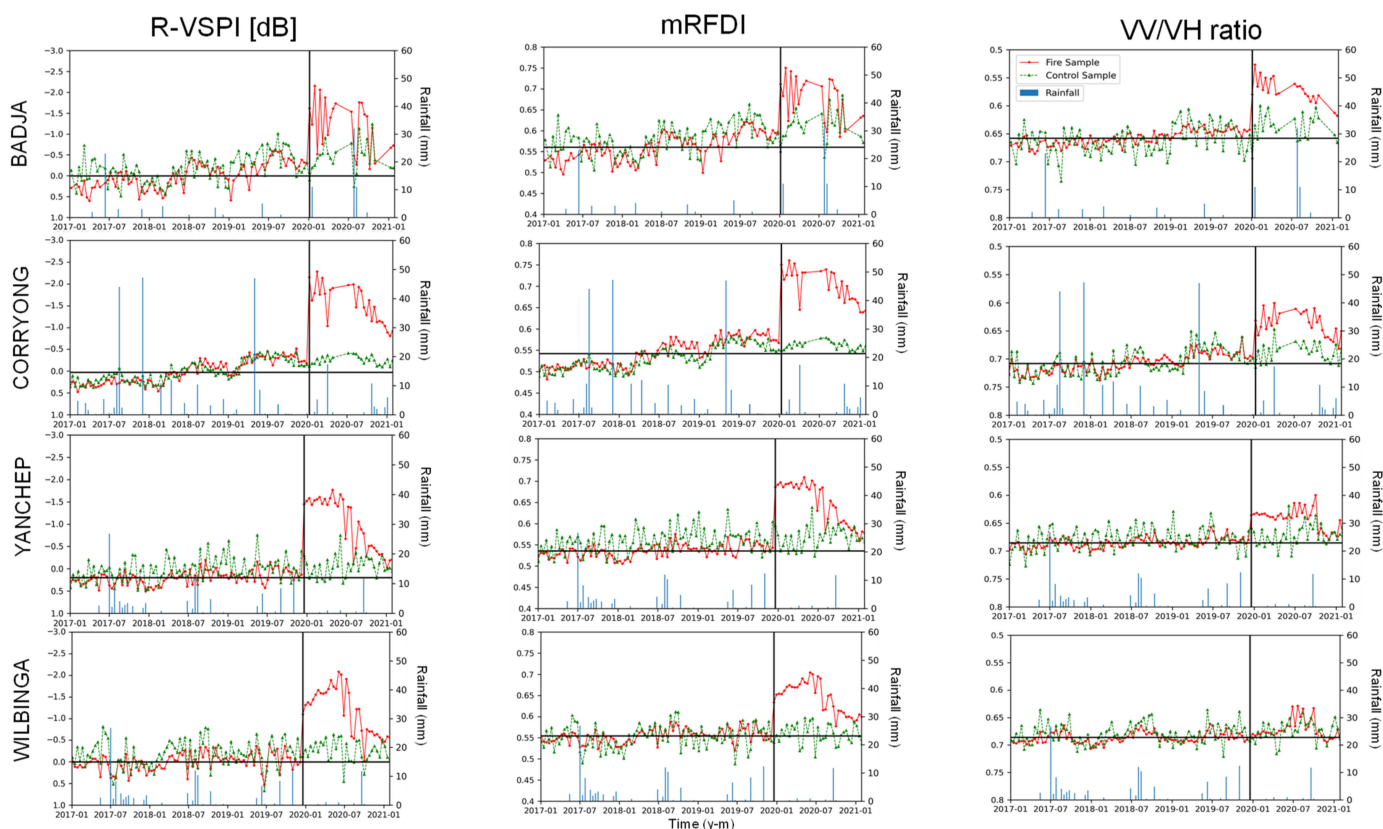

Figure 6. Four-year time series of R-VSPI, mRFDI, and VV/VH ratio using Sentinel-1 backscatter dataset for the other four selected wildfires. Data are shown for burnt/wildfire samples (red) and control samples (green). The black lines indicate the latest imagery post the wildfire event (vertical) and pre-fire conditions (horizontal, mean of the wildfire sample taken pre-fire). The rainfall data is shown in column bars (blue).

3.1.3. Spatio-Temporal Detection of Wildfire Scars from Sentinel-1

The Sentinel-1-based indices R-VSPI, mRFDI, and VV/VH ratio showed a heterogenous appearance due to speckle (coherent effect inherent to SAR observations) compared to Sentinel-2-based indices (VSPI, dNBR, and NDVI) (Figure 7). Nevertheless, all of these indices were successful in detecting the wildfire scars following the respective wildfire events. However, while the wildfire scars were still evident 11 months after an individual event using R-VSPI and mRFDI, the VV/VH ratio index showed largely recovered conditions post-fire. This trend agrees with that reflected in the time series of Figure 5a, where both R-VSPI and mRFDI were observed not to be returning to the same level as the undisturbed control sample while the VV/VH ratio values matched those of the control sample and the pre-fire conditions at that point in time. In comparison with mRFDI, the R-VSPI drops quicker towards recovery for wildfire scars (Timeline 5 and 7), but is still able to delineate the degradation for a longer period (11 months post-fire) (Figure 7). The lower values running seemingly along a line from north to south in the centre of the images is the local ridge between east- and westward facing slopes. The distinctive local difference in the indices compared to the surrounding area can be due to various effects ranging from different fire behaviour on the ridge, variations in vegetation, as well as the subsequent recovery. The latter is particularly noticeable in the optical indices that indicate a faster recovery on the west-facing slopes than the ones facing east (Figure 7).
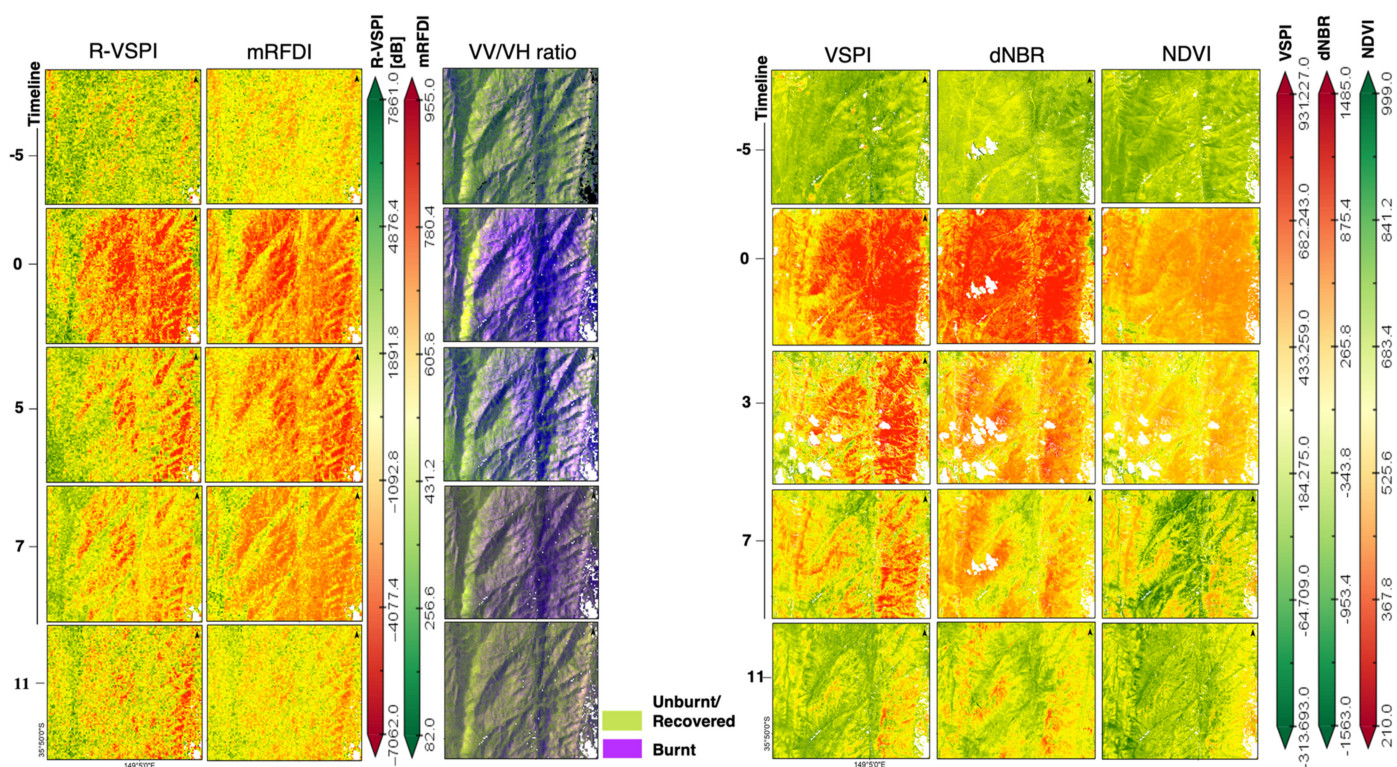
Figure 7. Multi-temporal comparison of SAR-based (R-VSPI, mRFDI, and VV/VH Ratio) and optical-based (VSPI, dNBR, and NDVI) vegetation indices for Orroral Valley wildfire that occurred in January–February 2020 in ACT. The colour maps for R-VSPI, mRFDI, VSPI, dNBR, and NDVI have been applied a linear stretch by a percent clip minimum and percent clip maximum value of 0.5. The VV/VH ratio maps are an RGB combination of the channels, red: VV, green: VH and blue: VV/VH, which signifies green as unburnt, and purple as burnt. The five scenes selected for optical include pre-fire scene: (i) 24 September 2019 (−5 months), closest date to the wildfire; (ii) 8 February 2020 (Timeline–0), and post-fire scenes; (iii) 15 July 2020 (5 months); and (iv) 18 September 2020 (7 months); and (v) 23 January 2021 (11 months). Similarly, the five scenes selected for optical indices include pre-fire scene (vi) 22 September 2019 (−5 months), closest date to the wildfire; (vii) 4 February 2020 (Timeline–0), and post-fire scenes; (viii) 15 May 2020 (3 months); (ix) 21 September 2020 (7 months); and (x) 19 January 2021 (11 months).

3.2. Sentinel-2 Analysis

3.2.1. Vegetation Lines from Sentinel-2

Figure 8 displays the multi-temporal correlation plots and subsequent vegetation lines for the same wildfires derived from the scaled surface reflectance bands (SWIR-1 and SWIR-2) of Sentinel-2 datasets. The regression slopes obtained for the Sentinel-2 data varied between the selected wildfires ranging from 0.71 for Corryong to 0.81 for the Wilbinga event, respectively. For the Wilbinga wildfire (WA) a higher vegetation line slope is attained from Sentinel-2 compared to the vegetation line slopes of other wildfires (Figure 8).

Figure 4b demonstrates an example of the (non-burnt) vegetation line (black) and the displaced burnt-area lines (colored) for the Orroral Valley wildfire (ACT) using the scaled surface reflectance values from Sentinel-2. The vegetation line (black) obtained from the paired scaled surface reflectance values over the forest areas from the pre-fire period represents undisturbed healthy vegetation (Figure 4b). The disturbance caused by wildfires shifted the post-fire scaled surface reflectance values away from the reference (vegetation) line, indicating the depletion of the forest fuel due to wildfire impact (Figure 4b). For the immediate post-fire period, the displaced isolines formed from the post-fire scaled surface reflectance values of Sentinel-2 showed a positive displacement from the vegetation line (Figure 4b). This is in accordance with the hypothesis (Figure 1A,C).
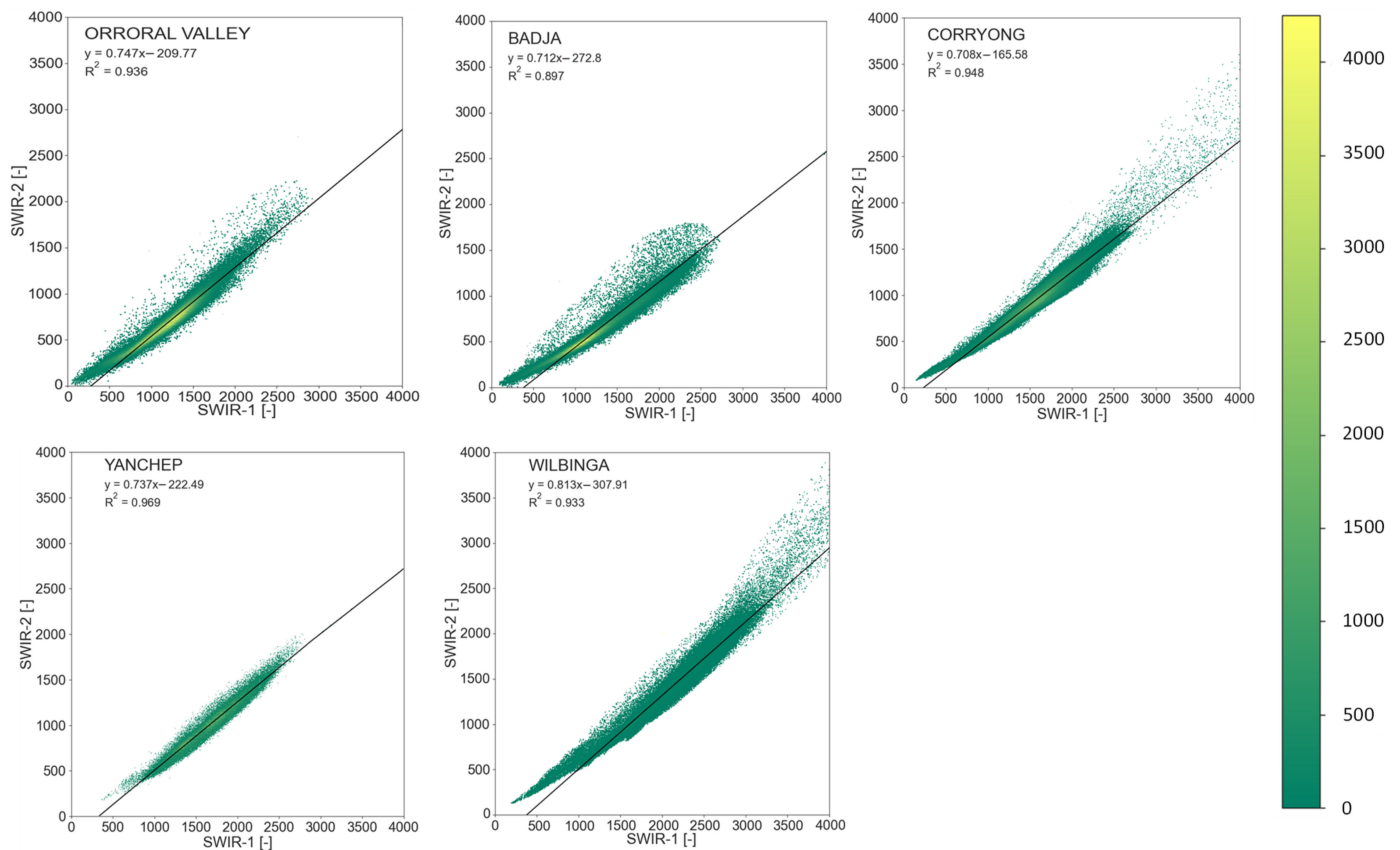
Figure 8. Density plots and linear vegetation lines from the scaled surface reflectance in the SWIR-1 (1.6 μm) and SWIR-2 (2.2 μm) bands from Sentinel-2 for different wildfires in South-Eastern Australia. Orroral Valley (Australian Capital Territory), Badja (New South Wales), Corryong (Victoria), Yanchep (Western Australia, and Wilbinga (Western Australia).

3.2.2. Analysis of Temporal Patterns from Sentinel-2

The VSPI, dNBR, and NDVI time-series derived from Sentinel-2 data for the respective study areas indicate that these indices can also distinguish the wildfire events by a clear deviation from the undisturbed vegetation conditions. Moreover, the difference between these indices and the undisturbed vegetation curve is able to track the potential post-fire vegetation recovery (Figures 5b and 9). However, the various Sentinel-2 based indices showed different time frames between them for the post-fire vegetation recovery.

The VSPI values calculated for the Orroral Valley wildfire (ACT) indicated that the disturbed vegetation still has not fully recovered (nearly reaching pre-fire conditions, meaning undisturbed vegetation line) 11 months after the fire occurrence (Figure 5b). However, for the same wildfire event the NDVI and dNBR values indicate full recovery of vegetation by reaching the pre-fire conditions in a period of 8 months (Figure 5b). A similar trend was also found for the Badja Forest fire (NSW), for which VSPI and dNBR showed signals for substantial recovery in a span of 12 months (Figure 9), while NDVI values indicated a much quicker recovery to pre-fire conditions. The reason may be attributed to the fact that the NIR-Red channel-based vegetation index, such as the NDVI, showed a quicker recovery during the post-fire period (reaching pre-fire conditions) due to the saturation of the optical signal, which may be due to both epicormic regrowth or understory recovery, and therefore could represent a mixed response [26]. For the Corryong, Yanchep, and Wilbinga wildfires, the post-fire temporal patterns of all indices do not reconcile with the undisturbed vegetation curve even 12 months after the wildfire. They exhibit a little change in the indices after extended time periods, indicating a stagnating recovery (Figure 9).
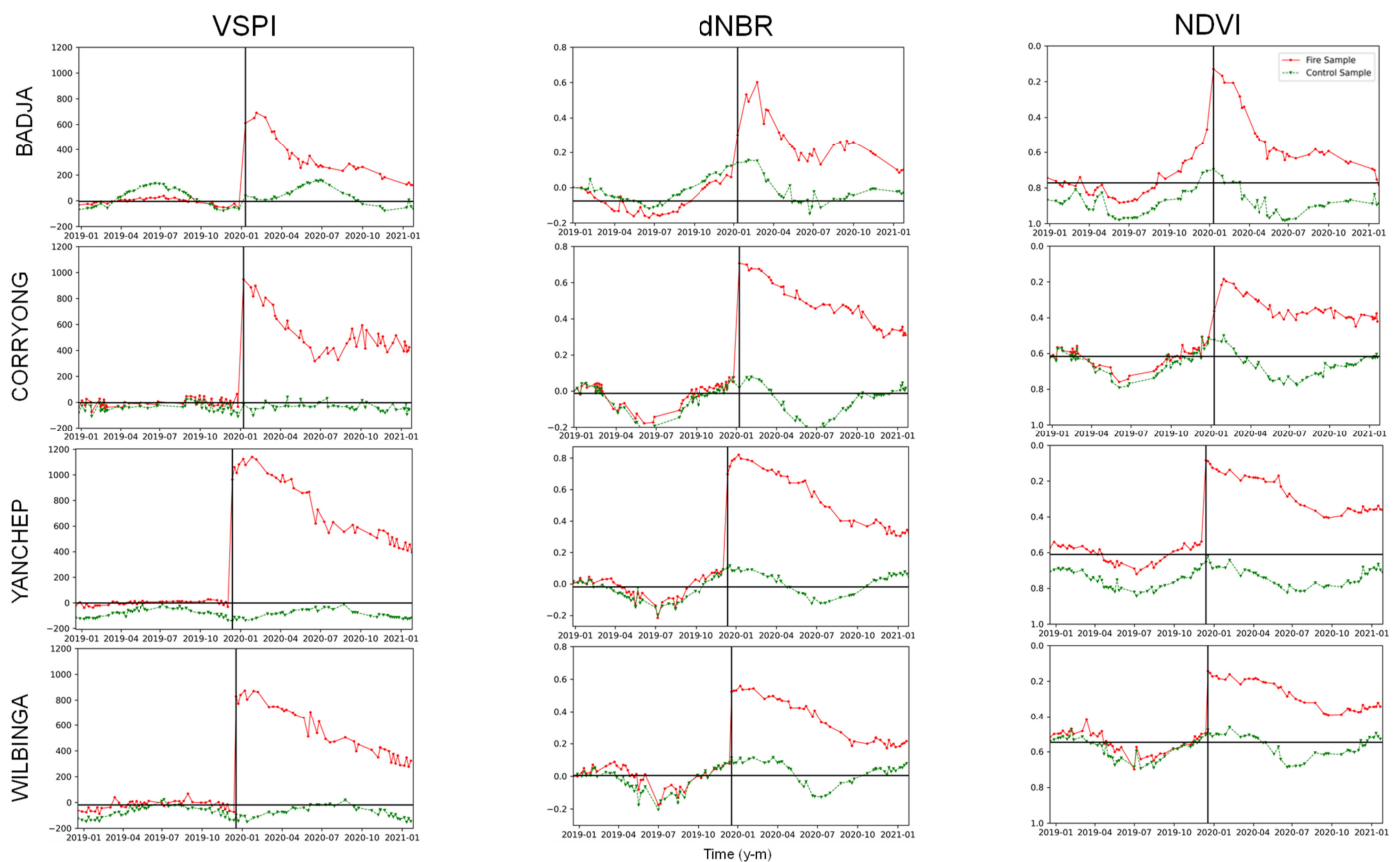
Figure 9. Two-year time series of VSPI, dNBR, and NDVI using Sentinel-2 scaled surface reflectance dataset for the other four selected wildfires. Data are shown for burnt/wildfire samples (red) and control samples (green). The black lines indicate the latest imagery post the wildfire event (vertical) and pre-fire conditions (horizontal, mean of the wildfire sample taken pre-fire).

In general, the VSPI control (undisturbed/unburnt) sample values are stable and varied around a steady-state value of 0, whereas the control sample values of dNBR and NDVI ranged in between −0.15 and 0.16 and 0.4 and 0.9, respectively (Figures 5b and 9). In addition, seasonal patterns in the control sample plots are visible in Badja, Yanchep, and Wilbinga (Figure 9). The dNBR and NDVI show some seasonality for the vegetation around the Orroral Valley (Figure 5b) and Corryong (Figure 9) study areas, while no substantial changes are evident in the VSPI.

3.2.3. Spatio-Temporal Detection of Wildfire Scars from Sentinel-2

The burnt area of the Orroral Valley wildfire is clearly visible for all the Sentinel-2-based indices, such as VSPI, dNBR, and NDVI (Timeline–0 in Figure 7). There was no clear delineation of areas with higher fire severity as with the radar indices, which may be due to the apparent saturation of the indices in the acquired data immediately following the wildfire event. The heterogeneity of the fire scarring started being clearly distinguishable in the VSPI, dNBR, and NDVI data about three months post-fire. While the wildfire scar was still delineated 11 months post-fire by VSPI and dNBR, the NDVI showed mostly recovered conditions from seven months post-fire. This trend agrees with that reflected in the time series of Figure 5b, where NDVI returned to the control sample and the pre-fire conditions.

3.3. Comparison of Sentinel-1 and Sentinel-2 Data Sensitivity towards Forest Fuel Condition

The density plots (Figures 3 and 8) show that the maximum number of points are concentrated along the vegetation line, for both sensor types. The high R2 values between the multi-temporal backscatter pairs of VV and VH polarization channels of Sentinel-1

(Figure 3) as well as scaled surface reflectance pairs of SWIR-2 and SWIR-1 of Sentinel-2 (Figure 8) for the selected wildfires indicate that most of the spatio-temporal variability of undisturbed vegetation is defined by the vegetation line. The clear orthogonal displacement for Sentinel-1 (Figure 4a) may be attributed to Sentinel-1 higher wavelength at C-band as compared to the SWIR bands from Sentinel-2 (Figure 4b), which allows deeper signal penetration into the vegetation canopy resulting in higher sensitivity towards internal structure layers within the affected vegetation canopy [43,77–79].

The post-fire temporal patterns Sentinel-1-based vegetation indices (Figure 5a—Orroral valley and Figure 6—Badja) showed that the vegetation was recovering after a wildfire at a slower rate compared to the Sentinel-2-based vegetation indices (Figure 5b—Orroral valley and Figure 9—Badja) and was still far from the pre-fire conditions. These differences in the recovery pattern may be indicating that the post-fire recovery shown by the VSPI might be tracking changes in the surface and near-surface fine fuels, such as tall and low shrubs, and dead and live grass in the understory [29], which often regrows more quickly than the over- and intermediate-story of the forest following a high intensity wildfire [80].

Mostly, the performance of R-VSPI for studying the temporal patterns of vegetation recovery in the case of the five wildfires was seen to be nearly the same in comparison to mRFDI and VV/VH ratio. In addition, the performance of R-VSPI in analyzing the post-fire temporal patterns is comparable to that of the VSPI. Using R-VSPI and VSPI in combination, rather than dNBR and mRFDI, may be advantageous as they have the same basic mathematical function. The strength of deriving both optical and radar indices using the same mathematical functions is in the simplicity of the formulation as well as the possibility to further explore complementarities in the derived indices, e.g., scaling is an option to transfer the data into a common numerical space to further investigate common (or complementary) behaviour over time. Any identified relationship could then lead to identifying the locally specific regrowth behaviour. Furthermore, once the relative changes between the indices are better understood, allometric transfer functions could be used for mutual gap-filling the derived data sets, which would be particularly useful during long periods of cloud cover, where SAR data can make full use of its all-weather capability. For the same duration, the recovery patterns from VSPI were quite distinct for the selected wildfires and are often caused by a mixture of drivers. For example, the post-fire vegetation recovery in Orroral Valley (Figure 5b) and Badja (Figure 9) wildfires were more sudden and linear, perhaps signaling a different recovery pathway as a result of potentially more favorable weather conditions. This was the case with the Australian 2019/2020 "Black Summer" wildfire season that followed an extreme drought in 2019 and ended with rainfall events across south-eastern Australia [81]. Rainfall during the acquisition, intercepted water, and soil moisture are likely to have an impact on the radar-based metrics. However, the impact is unlikely to have a long-term effect, and hence was not discussed in detail in this paper. All the indices could also detect the wildfire scars in the scenes immediate to the wildfire event (spikes in Figures 5, 6 and 9, clear red/yellow/purple patches in Figure 7). The extent of the disturbance captured by all the indices varied across different wildfire events for the same index (Figures 5, 6 and 9).

Comparing the two sensors, SAR (Sentinel-1) was able to offer a dense time-series of pre- and post-fire acquisitions (due to its insensitivity towards cloud cover) and better spatio-temporal variability compared against optical (Sentinel-2) data, which has to be filtered for cloud-free scenes (Table 1). Previous studies have also shown that SAR has higher sensitivity towards the vegetation structure providing more detail to the impact of the wildfire and recovery compared to the traditional indices applied to optical data [82], whereas optical and infrared data has higher sensitivity towards leaf area index [83], and leaf tissues and photosynthetic activity [84]. This presents the complementary and convergent nature of the two different datasets. Due to the complementarity of SAR and optical remote sensing, and sensitivities to fuel structure and biomass, a future line of work may investigate combining the VSPI in a joint SAR-optics framework to generate an enhanced signal that may provide a better assessment towards fire-affected vertical fuel

strata and the subsequent recovery. Availability of adequate field data related to fuel load will assist in validation, which is a limitation of this study.

4. Conclusions

The VSPI is a perpendicular index that estimates wildfire impact on the forest and post-fire vegetation recovery using shortwave-infrared spectral bands from Sentinel-2 (centered at 1.6 µm and 2.2 µm). A novel SAR-based index, R-VSPI was developed using polarization channels from Sentinel-1 (center wavelength at 5 cm) for quantifying changes in fuel load due to wildfires. The results indicate that SAR- and optical-based indices are able to reliably identify the wildfire events with a clear deviation from undisturbed vegetation conditions. R-VSPI and VSPI show their ability to estimate the wildfire-induced forest changes as the orthogonal distance from a linear reference line that characterized the undisturbed forest. Transferring the VSPI metric to Sentinel-1 (R-VSPI) provides complementary information for the assessment of wildfire disturbance and recovery of the fuel structure in a forested area over a longer duration than the VSPI on Sentinel-2 and the other widely used ratio-based indices, such as the dNBR and NDVI. The input observations required for estimation of R-VSPI and VSPI are freely available by ESA's Copernicus program. The two satellite missions considered in this paper provide gridded data at a spatial resolution of 10 m (Sentinel-1; SAR) and at 20 m (Sentinel-2; optical), respectively. The Sentinel-1 C-band SAR backscatter has proven to be sensitive to fire-induced changes in forest (eucalyptus) vegetation. The expected launch of L-Band (1.25 GHz) SAR satellite (e.g., the NASA/ISRO Synthetic Aperture RADAR (NISAR); [85]) and P-Band (0.43 GHz) SAR satellite (ESA's Biomass; [86]) with higher revisits in the near future could provide more opportunities for the application of R-VSPI on higher SAR wavelengths that can perform large-scale fuel load structure mapping in dense canopies due to higher canopy penetration. If appropriately interpreted, fuel load maps produced by R-VSPI may have applications beyond wildfire risk assessment, particularly in measuring other forest disturbances due to drought, logging, or disease.

Author Contributions: Conceptualization, C.R., A.C., J.H. and M.Y.; methodology, A.C., C.R., J.H., T.J. and M.Y.; software, A.C.; formal analysis, A.C., C.R. and T.J.; data curation, A.C., C.R. and T.J.; writing—original draft preparation, A.C.; writing—review and editing, A.C., C.R., M.Y., T.J. and J.H. All authors have read and agreed to the published version of the manuscript.

Data Availability Statement: Data sharing not applicable.

Conflicts of Interest: The authors declare no conflict of interest.

References

1. Bowman, D.M.; Balch, J.K.; Artaxo, P.; Bond, W.J.; Carlson, J.M.; Cochrane, M.A.; D'Antonio, C.M.; DeFries, R.S.; Doyle, J.C.; Harrison, S.P. Fire in the Earth system. *Science* **2009**, *324*, 481–484. [CrossRef] [PubMed]
2. Giglio, L.; Boschetti, L.; Roy, D.P.; Humber, M.L.; Justice, C.O. The Collection 6 MODIS burned area mapping algorithm and product. *Remote Sens. Environ.* **2018**, *217*, 72–85. [CrossRef] [PubMed]
3. Abreu, R.C.; Hoffmann, W.A.; Vasconcelos, H.L.; Pilon, N.A.; Rossatto, D.R.; Durigan, G. The biodiversity cost of carbon sequestration in tropical savanna. *Sci. Adv.* **2017**, *3*, e1701284. [CrossRef] [PubMed]
4. Rogers, B.M.; Balch, J.K.; Goetz, S.J.; Lehmann, C.E.; Turetsky, M. Focus on changing fire regimes: Interactions with climate, ecosystems, and society. *Environ. Res. Lett.* **2020**, *15*, 30201. [CrossRef]
5. Tolhurst, K. Prescribed burning in Victoria: Policy and practice. In Proceedings of the Bushfire Prevention: Are We Doing Enough? Conference, Melbourne, VIC, Australia, 11 March 2003.
6. Pyne, S. *The Still-Burning Bush: Updated Edition*; Scribe Publications: Melbourne, Australia, 2020.
7. Chuvieco, E.; Aguado, I.; Jurdao, S.; Pettinari, M.L.; Yebra, M.; Salas, J.; Hantson, S.; De la Riva, J.; Ibarra, P.; Rodrigues, M. Integrating geospatial information into fire risk assessment. *Int. J. Wildland Fire* **2012**, *23*, 606–619. [CrossRef]
8. Yebra, M.; Quan, X.; Riaño, D.; Larraondo, P.R.; Van Dijk, A.I.; Cary, G.J. A fuel moisture content and flammability monitoring methodology for continental Australia based on optical remote sensing. *Remote Sens. Environ.* **2018**, *212*, 260–272. [CrossRef]
9. Miller, C.; Ager, A.A. A review of recent advances in risk analysis for wildfire management. *Int. J. Wildland Fire* **2012**, *22*, 1–14. [CrossRef]

10. Preisler, H.K.; Brillinger, D.R.; Burgan, R.E.; Benoit, J. Probability based models for estimation of wildfire risk. *Int. J. Wildland Fire* **2004**, *13*, 133–142. [CrossRef]
11. Gould, J.S.; McCaw, W.L.; Cheney, N.P. Quantifying fine fuel dynamics and structure in dry eucalypt forest (Eucalyptus marginata) in Western Australia for fire management. *For. Ecol. Manag.* **2011**, *262*, 531–546. [CrossRef]
12. Hilton, J.E.; Miller, C.; Sullivan, A.L.; Rucinski, C. Effects of spatial and temporal variation in environmental conditions on simulation of wildfire spread. *Environ. Model. Softw.* **2015**, *67*, 118–127. [CrossRef]
13. Hilton, J.; Miller, C.; Sharples, J.; Sullivan, A. Curvature effects in the dynamic propagation of wildfires. *Int. J. Wildland Fire* **2016**, *25*, 1238–1251. [CrossRef]
14. Lopes, A.; Cruz, M.G.; Viegas, D. FireStation—An integrated software system for the numerical simulation of fire spread on complex topography. *Environ. Model. Softw.* **2002**, *17*, 269–285. [CrossRef]
15. Perry, G.L.; Sparrow, A.D.; Owens, I.F. A GIS-supported model for the simulation of the spatial structure of wildland fire, Cass Basin, New Zealand. *J. Appl. Ecol.* **1999**, *36*, 502–518. [CrossRef]
16. Zylstra, P.; Bradstock, R.A.; Bedward, M.; Penman, T.D.; Doherty, M.D.; Weber, R.O.; Gill, A.M.; Cary, G.J. Biophysical mechanistic modelling quantifies the effects of plant traits on fire severity: Species, not surface fuel loads, determine flame dimensions in eucalypt forests. *PLoS ONE* **2016**, *11*, e0160715. [CrossRef]
17. Atchley, A.L.; Linn, R.; Jonko, A.; Hoffman, C.; Hyman, J.D.; Pimont, F.; Sieg, C.; Middleton, R.S. Effects of fuel spatial distribution on wildland fire behaviour. *Int. J. Wildland Fire* **2021**, *30*, 179–189. [CrossRef]
18. Duff, T.J.; Chong, D.M.; Tolhurst, K.G. Quantifying spatio-temporal differences between fire shapes: Estimating fire travel paths for the improvement of dynamic spread models. *Environ. Model. Softw.* **2013**, *46*, 33–43. [CrossRef]
19. Taneja, R.; Hilton, J.; Wallace, L.; Reinke, K.; Jones, S. Effect of fuel spatial resolution on predictive wildfire models. *Int. J. Wildland Fire* **2021**, *30*, 776–789. [CrossRef]
20. Wilson, A. *Assessing Fire Hazard on Public Lands in Victoria: Fire Management Needs, and Practical Research Objectives*; Department of Conservation and Environment: Melbourne, VIC, Australia, 1992.
21. Holmes, A.W.; Rüdiger, C.; Harris, S.; Tapper, N. Determining the minimum sampling frequency for ground measurements of burn severity. *Int. J. Wildland Fire* **2018**, *27*, 387–395. [CrossRef]
22. Tiribelli, F.; Kitzberger, T.; Morales, J.M. Changes in vegetation structure and fuel characteristics along post-fire succession promote alternative stable states and positive fire–vegetation feedbacks. *J. Veg. Sci.* **2018**, *29*, 147–156. [CrossRef]
23. Szpakowski, D.M.; Jensen, J.L. A review of the applications of remote sensing in fire ecology. *Remote Sens.* **2019**, *11*, 2638. [CrossRef]
24. Chen, X.; Vogelmann, J.E.; Rollins, M.; Ohlen, D.; Key, C.H.; Yang, L.; Huang, C.; Shi, H. Detecting post-fire burn severity and vegetation recovery using multitemporal remote sensing spectral indices and field-collected composite burn index data in a ponderosa pine forest. *Int. J. Remote Sens.* **2011**, *32*, 7905–7927. [CrossRef]
25. Meng, R.; Wu, J.; Schwager, K.L.; Zhao, F.; Dennison, P.E.; Cook, B.D.; Brewster, K.; Green, T.M.; Serbin, S.P. Using high spatial resolution satellite imagery to map forest burn severity across spatial scales in a Pine Barrens ecosystem. *Remote Sens. Environ.* **2017**, *191*, 95–109. [CrossRef]
26. Chu, T.; Guo, X. Remote sensing techniques in monitoring post-fire effects and patterns of forest recovery in boreal forest regions: A review. *Remote Sens.* **2013**, *6*, 470–520. [CrossRef]
27. Escuin, S.; Navarro, R.; Fernandez, P. Fire severity assessment by using NBR (Normalized Burn Ratio) and NDVI (Normalized Difference Vegetation Index) derived from LANDSAT TM/ETM images. *Int. J. Remote Sens.* **2008**, *29*, 1053–1073. [CrossRef]
28. Harris, S.; Veraverbeke, S.; Hook, S. Evaluating spectral indices for assessing fire severity in chaparral ecosystems (Southern California) using MODIS/ASTER (MASTER) airborne simulator data. *Remote Sens.* **2011**, *3*, 2403–2419. [CrossRef]
29. Massetti, A.; Rüdiger, C.; Yebra, M.; Hilton, J. The Vegetation Structure Perpendicular Index (VSPI): A forest condition index for wildfire predictions. *Remote Sens. Environ.* **2019**, *224*, 167–181. [CrossRef]
30. Rouse, J., Jr.; Haas, R.H.; Deering, D.; Schell, J.; Harlan, J.C. *Monitoring the Vernal Advancement and Retrogradation (Green Wave Effect) of Natural Vegetation*; No. NASA-CR-132982; NASA: Washington, DC, USA, 1974.
31. García, M.L.; Caselles, V. Mapping burns and natural reforestation using Thematic Mapper data. *Geocarto Int.* **1991**, *6*, 31–37. [CrossRef]
32. Key, C. Landscape assessment (LA): Sampling and analysis methods. In *FIREMON: Fire Effects Monitoring and Inventory System*; Lutes, D.C., Keane, R.E., Caratti, J.F., Key, C.H., Benson, N.C., Sutherland, S., Gangi, L.J., Eds.; General Technical Report RMRS-GTR-164; USDA Forest Service, Rocky Mountain Research Station: Fort Collins, CO, USA, 2006; pp. LA1–LA51.
33. Roy, D.P.; Boschetti, L.; Trigg, S.N. Remote sensing of fire severity: Assessing the performance of the normalized burn ratio. *IEEE Geosci. Remote Sens. Lett.* **2006**, *3*, 112–116. [CrossRef]
34. Gale, M.G.; Cary, G.J.; Yebra, M.; Leavesley, A.J.; Van Dijk, A.I. Comparison of contrasting optical and LiDAR fire severity remote sensing methods in a heterogeneous forested landscape in south-eastern Australia. *Int. J. Remote Sens.* **2022**, *43*, 2559–2580. [CrossRef]
35. Parks, S.A.; Dillon, G.K.; Miller, C. A new metric for quantifying burn severity: The relativized burn ratio. *Remote Sens.* **2014**, *6*, 1827–1844. [CrossRef]
36. Hoy, E.E.; French, N.H.; Turetsky, M.R.; Trigg, S.N.; Kasischke, E.S. Evaluating the potential of Landsat TM/ETM+ imagery for assessing fire severity in Alaskan black spruce forests. *Int. J. Wildland Fire* **2008**, *17*, 500–514. [CrossRef]

37. Addison, P.; Oommen, T. Utilizing satellite radar remote sensing for burn severity estimation. *Int. J. Appl. Earth Obs. Geoinf.* **2018**, *73*, 292–299. [CrossRef]

38. Tanase, M.A.; Santoro, M.; De La Riva, J.; Fernando, P.; Le Toan, T. Sensitivity of X-, C-, and L-band SAR backscatter to burn severity in Mediterranean pine forests. *IEEE Trans. Geosci. Remote Sens.* **2010**, *48*, 3663–3675. [CrossRef]

39. Zhou, Z.; Liu, L.; Jiang, L.; Feng, W.; Samsonov, S.V. Using long-term SAR backscatter data to monitor post-fire vegetation recovery in tundra environment. *Remote Sens.* **2019**, *11*, 2230. [CrossRef]

40. Rao, K.; Williams, A.P.; Flefil, J.F.; Konings, A.G. SAR-enhanced mapping of live fuel moisture content. *Remote Sens. Environ.* **2020**, *245*, 111797. [CrossRef]

41. Tian, F.; Brandt, M.; Liu, Y.Y.; Verger, A.; Tagesson, T.; Diouf, A.A.; Rasmussen, K.; Mbow, C.; Wang, Y.; Fensholt, R. Remote sensing of vegetation dynamics in drylands: Evaluating vegetation optical depth (VOD) using AVHRR NDVI and in situ green biomass data over West African Sahel. *Remote Sens. Environ.* **2016**, *177*, 265–276. [CrossRef]

42. Ulaby, F.T.; Long, D.G.; Blackwell, W.J.; Elachi, C.; Fung, A.K.; Ruf, C.; Sarabandi, K.; Zebker, H.A.; Van Zyl, J. *Microwave Radar and Radiometric Remote Sensing*; University of Michigan Press: Ann Arbor, MI, USA, 2014; Volume 4.

43. Tanase, M.A.; Santoro, M.; Wegmüller, U.; De la Riva, J.; Pérez-Cabello, F. Properties of X-, C-and L-band repeat-pass interferometric SAR coherence in Mediterranean pine forests affected by fires. *Remote Sens. Environ.* **2010**, *114*, 2182–2194. [CrossRef]

44. Kasischke, E.S.; Tanase, M.A.; Bourgeau-Chavez, L.L.; Borr, M. Soil moisture limitations on monitoring boreal forest regrowth using spaceborne L-band SAR data. *Remote Sens. Environ.* **2011**, *115*, 227–232. [CrossRef]

45. Tanase, M.; Kennedy, R.; Aponte, C. Radar Burn Ratio for fire severity estimation at canopy level: An example for temperate forests. *Remote Sens. Environ.* **2015**, *170*, 14–31. [CrossRef]

46. Tanase, M.A.; Villard, L.; Pitar, D.; Apostol, B.; Petrila, M.; Chivulescu, S.; Leca, S.; Borlaf-Mena, I.; Pascu, I.-S.; Dobre, A.-C. Synthetic aperture radar sensitivity to forest changes: A simulations-based study for the Romanian forests. *Sci. Total Environ.* **2019**, *689*, 1104–1114. [CrossRef]

47. Tanase, M.; De la Riva, J.; Santoro, M.; Pérez-Cabello, F.; Kasischke, E. Sensitivity of SAR data to post-fire forest regrowth in Mediterranean and boreal forests. *Remote Sens. Environ.* **2011**, *115*, 2075–2085. [CrossRef]

48. Liao, Z.; Van Dijk, A.I.; He, B.; Larraondo, P.R.; Scarth, P.F. Woody vegetation cover, height and biomass at 25-m resolution across Australia derived from multiple site, airborne and satellite observations. *Int. J. Appl. Earth Obs. Geoinf.* **2020**, *93*, 102209. [CrossRef]

49. Curran, P.J. Remote sensing of foliar chemistry. *Remote Sens. Environ.* **1989**, *30*, 271–278. [CrossRef]

50. Kollenkark, J.; Vanderbilt, V.; Daughtry, C.; Bauer, M. Influence of solar illumination angle on soybean canopy reflectance. *Appl. Opt.* **1982**, *21*, 1179–1184. [CrossRef]

51. Richardson, A.J.; Wiegand, C. Distinguishing vegetation from soil background information. *Photogramm. Eng. Remote Sens.* **1977**, *43*, 1541–1552.

52. Verstraete, M.M.; Pinty, B. Designing optimal spectral indexes for remote sensing applications. *IEEE Trans. Geosci. Remote Sens.* **1996**, *34*, 1254–1265. [CrossRef]

53. Saatchi, S. SAR methods for mapping and monitoring forest biomass. In *SAR Handbook: Comprehensive Methodologies for Forest Monitoring and Biomass Estimation*; Flores, A., Herndon, K., Thapa, R., Cherrington, E., Eds.; NASA: Washington, DC, USA, 2019; pp. 207–246.

54. Cloude, S.R.; Pottier, E. An entropy based classification scheme for land applications of polarimetric SAR. *IEEE Trans. Geosci. Remote Sens.* **1997**, *35*, 68–78. [CrossRef]

55. Morgan, G.; Tolhurst, K.; Poynter, M.; Cooper, N.; McGuffog, T.; Ryan, R.; Wouters, M.; Stephens, N.; Black, P.; Sheehan, D. Prescribed burning in south-eastern Australia: History and future directions. *Aust. For.* **2020**, *83*, 4–28. [CrossRef]

56. Dinerstein, E.; Olson, D.; Joshi, A.; Vynne, C.; Burgess, N.D.; Wikramanayake, E.; Hahn, N.; Palminteri, S.; Hedao, P.; Noss, R. An ecoregion-based approach to protecting half the terrestrial realm. *BioScience* **2017**, *67*, 534–545. [CrossRef]

57. Fox-Hughes, P.; Yebra, M.; Kumar, V.; Dowdy, A.; Hope, P.; Peace, M.; Narsey, S.; Shokirov, S.; Delage, F.; Zhang, H. *Soil and Fuel Moisture Precursors of Fire Activity during the 2019–20 Fire Season, in Comparison to Previous Seasons—Black Summer Final Report*; Bushfire and Natural Hazards CRC: Melbourne, Australia, 2021.

58. Baldwin, C.; Ross, H. *Beyond a Tragic Fire Season: A Window of Opportunity to Address Climate Change?* Taylor & Francis: Abingdon, UK, 2020; Volume 27, pp. 1–5.

59. Bowman, D.; Williamson, G.; Yebra, M.; Lizundia-Loiola, J.; Pettinari, M.L.; Shah, S.; Bradstock, R.; Chuvieco, E. *Wildfires: Australia Needs National Monitoring Agency*; Nature Publishing Group: London, UK, 2020.

60. Deb, P.; Moradkhani, H.; Abbaszadeh, P.; Kiem, A.S.; Engström, J.; Keellings, D.; Sharma, A. Causes of the widespread 2019–2020 Australian bushfire season. *Earth's Future* **2020**, *8*, e2020EF001671. [CrossRef]

61. Hughes, L.; Steffen, W.; Mullins, G.; Dean, A.; Weisbrot, E.; Rice, M. *Summer of Crisis*; Climate Council of Australia Limited: Melbourne, Australia, 2020.

62. Forestry, C.D.o.; Protection, F. *Community Wildfire Prevention & Mitigation Report*; CalFire Resource and Assessment Program: California, CA, USA, 2019.

63. Boer, M.M.; Resco de Dios, V.; Bradstock, R.A. Unprecedented burn area of Australian mega forest fires. *Nat. Clim. Chang.* **2020**, *10*, 171–172. [CrossRef]

64. Davey, S.M.; Sarre, A. *The 2019/20 Black Summer Bushfires*; Taylor & Francis: Abingdon, UK, 2020; Volume 83, pp. 47–51.

65. Commonwealth of Australia. *Royal Commission into National Natural Disaster Arrangements Report*; Royal Commission into National Natural Disaster Arrangements Canberra: Canberra, Australia, 2020.

66. Torres, R.; Snoeij, P.; Geudtner, D.; Bibby, D.; Davidson, M.; Attema, E.; Potin, P.; Rommen, B.; Floury, N.; Brown, M. GMES Sentinel-1 mission. *Remote Sens. Environ.* **2012**, *120*, 9–24. [CrossRef]

67. Google Earth Engine: Sentinel-1. Available online: https://developers.google.com/earth-engine/sentinel1 (accessed on 19 October 2021).

68. Lee, J.-S.; Jurkevich, L.; Dewaele, P.; Wambacq, P.; Oosterlinck, A. Speckle filtering of synthetic aperture radar images: A review. *Remote Sens. Rev.* **1994**, *8*, 313–340. [CrossRef]

69. Drusch, M.; Del Bello, U.; Carlier, S.; Colin, O.; Fernandez, V.; Gascon, F.; Hoersch, B.; Isola, C.; Laberinti, P.; Martimort, P. Sentinel-2: ESA's optical high-resolution mission for GMES operational services. *Remote Sens. Environ.* **2012**, *120*, 25–36. [CrossRef]

70. Google Earth Engine: Sentinel-2. Available online: https://developers.google.com/earth-engine/datasets/catalog/COPERNICUS_S2_SR (accessed on 19 October 2021).

71. Mitchard, E.T.; Saatchi, S.S.; White, L.J.; Abernethy, K.A.; Jeffery, K.J.; Lewis, S.L.; Collins, M.; Lefsky, M.A.; Leal, M.E.; Woodhouse, I.H. Mapping tropical forest biomass with radar and spaceborne LiDAR in Lopé National Park, Gabon: Overcoming problems of high biomass and persistent cloud. *Biogeosciences* **2012**, *9*, 179–191. [CrossRef]

72. Symeonakis, E.; Higginbottom, T.P.; Petroulaki, K.; Rabe, A. Optimisation of savannah land cover characterisation with optical and SAR data. *Remote Sens.* **2018**, *10*, 499. [CrossRef]

73. Nicolau, A.P.; Flores-Anderson, A.; Griffin, R.; Herndon, K.; Meyer, F.J. Assessing SAR C-band data to effectively distinguish modified land uses in a heavily disturbed Amazon forest. *Int. J. Appl. Earth Obs. Geoinf.* **2021**, *94*, 102214. [CrossRef]

74. Gill, A.M. *Bushfires and Biodiversity in Southern Australian Forests*; CSIRO Publishing: Melbourne, Australia, 2012.

75. Alpers, W.; Zhang, B.; Mouche, A.; Zeng, K.; Chan, P.W. Rain footprints on C-band synthetic aperture radar images of the ocean-Revisited. *Remote Sens. Environ.* **2016**, *187*, 169–185. [CrossRef]

76. Grover, K.; Quegan, S.; Da Costa Freitas, C. Quantitative estimation of tropical forest cover by SAR. *IEEE Trans. Geosci. Remote Sens.* **1999**, *37*, 479–490. [CrossRef]

77. Jagdhuber, T.; Montzka, C.; Lopez-Martinez, C.; Baur, M.J.; Link, M.; Piles, M.; Das, N.N.; Jonard, F. Estimation of vegetation structure parameters from SMAP radar intensity observations. *IEEE Trans. Geosci. Remote Sens.* **2020**, *59*, 151–167. [CrossRef]

78. Kasischke, E.S.; Bourgeau-Chavez, L.L.; Johnstone, J.F. Assessing spatial and temporal variations in surface soil moisture in fire-disturbed black spruce forests in Interior Alaska using spaceborne synthetic aperture radar imagery—Implications for post-fire tree recruitment. *Remote Sens. Environ.* **2007**, *108*, 42–58. [CrossRef]

79. Liu, P.-W.; Judge, J.; De Roo, R.D.; England, A.W.; Bongiovanni, T. Uncertainty in soil moisture retrievals using the SMAP combined active–passive algorithm for growing sweet corn. *IEEE J. Sel. Top. Appl. Earth Obs. Remote Sens.* **2016**, *9*, 3326–3339. [CrossRef]

80. Barker, J.W.; Price, O.F. Positive severity feedback between consecutive fires in dry eucalypt forests of southern Australia. *Ecosphere* **2018**, *9*, e02110. [CrossRef]

81. Kemter, M.; Fischer, M.; Luna, L.V.; Schönfeldt, E.; Vogel, J.; Banerjee, A.; Korup, O.; Thonicke, K. Cascading hazards in the aftermath of Australia's 2019/2020 Black Summer wildfires. *Earth's Future* **2021**, *9*, e2020EF001884. [CrossRef]

82. Minchella, A.; Del Frate, F.; Capogna, F.; Anselmi, S.; Manes, F. Use of multitemporal SAR data for monitoring vegetation recovery of Mediterranean burned areas. *Remote Sens. Environ.* **2009**, *113*, 588–597. [CrossRef]

83. Carlson, T.N.; Ripley, D.A. On the relation between NDVI, fractional vegetation cover, and leaf area index. *Remote Sens. Environ.* **1997**, *62*, 241–252. [CrossRef]

84. Asner, G.P. Biophysical and biochemical sources of variability in canopy reflectance. *Remote Sens. Environ.* **1998**, *64*, 234–253. [CrossRef]

85. Rosen, P.A.; Hensley, S.; Shaffer, S.; Veilleux, L.; Chakraborty, M.; Misra, T.; Bhan, R.; Sagi, V.R.; Satish, R. The NASA-ISRO SAR mission-An international space partnership for science and societal benefit. In Proceedings of the 2015 IEEE Radar Conference (RadarCon), Arlington, VA, USA, 10–15 May 2015; pp. 1610–1613.

86. Quegan, S.; Le Toan, T.; Chave, J.; Dall, J.; Exbrayat, J.-F.; Minh, D.H.T.; Lomas, M.; D'Alessandro, M.M.; Paillou, P.; Papathanassiou, K. The European Space Agency BIOMASS mission: Measuring forest above-ground biomass from space. *Remote Sens. Environ.* **2019**, *227*, 44–60. [CrossRef]